Graphical Abstract

Vortex Rope Morphology Controls Runner Fatigue Failure Mode: An Analytical Framework Linking Draft Tube Flow Physics to Blade Life Prediction in Francis Turbines

Jianxu Jiang, Reihani Rosti

Highlights

Vortex Rope Morphology Controls Runner Fatigue Failure Mode: An Analytical Framework Linking Draft Tube Flow Physics to Blade Life Prediction in Francis Turbines

Sanaz Zang, Rodnei Roos

- Different vortex rope morphologies excite different runner vibration modes
- Helical, columnar, and double-helix ropes concentrate stress at distinct blade locations
- Operating condition determines fatigue failure mode, not merely failure rate
- One-way FSI is justified: blade deformations are five orders of magnitude below draft tube scales
- Condition monitoring must track pressure phase distribution, not only amplitude

Vortex Rope Morphology Controls Runner Fatigue Failure Mode: An Analytical Framework Linking Draft Tube Flow Physics to Blade Life Prediction in Francis Turbines

Jiaxin Jiang[1,*], Barbara Ruiz[1]

[1]Department of Engineering Science, University of Oxford, Parks Road, Oxford, OX1 3PJ, United Kingdom

Abstract

Francis turbines operating off-design develop distinct draft-tube vortex rope morphologies—helical at part-load, columnar at overload, and double-helix at deep part-load—that generate pressure pulsations with different circumferential phase distributions. While prior fatigue assessments typically treat operating conditions as affecting only pulsation amplitude, the phase pattern determines which runner vibration mode is excited and therefore where stress concentrates. This paper presents an analytical framework that links idealized $m = 0/1/2$ pressure phase patterns to mode-dependent runner stress and fatigue-life estimates using one-way FSI and rain-flow damage accumulation, calibrated with published experimental and 3-D FEA evidence. The framework predicts three distinct failure mechanisms: trailing-edge fatigue at part-load, negligible damage at overload (below endurance limit), and leading-edge risk at deep part-load. The results imply that condition monitoring must track phase content, not only amplitude, and that reinforcement should be tailored to the expected operating profile.

Keywords: Francis turbine, vortex rope, draft tube cavitation, fluid-structure interaction, fatigue life, pressure pulsation

1. Introduction

The global transition toward intermittent renewable sources has fundamentally changed the role of hydropower. Turbines originally designed

*Corresponding author

Email addresses: jiaxin.jiang@eng.ox.ac.uk (Jiaxin Jiang), barbara.ruiz@eng.ox.ac.uk (Barbara Ruiz)

for steady baseload operation are now required to provide grid-balancing services—load following, frequency regulation, and spinning reserve—that demand rapid and frequent excursions to off-design operating conditions [2]. Francis turbines, which account for approximately 60% of installed hydropower capacity worldwide, are particularly affected because their fixed-geometry runners produce strongly off-design swirling flow at the draft tube inlet when operating away from the best-efficiency point (BEP). The resulting flow instabilities shorten runner life and increase maintenance costs, creating a tension between the flexibility demands of modern grids and the structural integrity of existing turbine fleets.

The dominant flow instability at off-design conditions is the vortex rope: a coherent low-pressure structure that forms in the draft tube when the residual swirl from the runner undergoes vortex breakdown [3]. Three canonical morphologies are observed depending on the operating condition. At part-load (60–85% of BEP discharge), a single helical vortex rope precesses around the draft tube axis at 0.2–0.4 times the runner frequency, generating a rotating pressure wave [3, 4]. At overload (above ~110% BEP), the helical structure is replaced by an axisymmetric columnar vortex that pulsates radially [5]. At deep part-load (below ~45% BEP), the single helix transitions to a double-helix structure consisting of two intertwined vortex filaments [6, 7]. Each morphology produces qualitatively different pressure pulsation patterns on the runner blades.

The link between vortex-rope-induced pressure pulsations and runner fatigue has been the subject of extensive research. Susan-Resiga et al. [3] established the analytical framework connecting swirl parameters to vortex breakdown topology. The Francis-99 workshops provided benchmark experimental and numerical data for a model Francis turbine across operating conditions [8, 9]. On the structural side, Rodriguez et al. [9] and Liang et al. [10] characterized the modal behaviour of submerged runners, demonstrating that added-mass effects reduce natural frequencies by up to 44%. Fluid-structure interaction studies by Trivedi et al. [11, 12] and Liu et al. [13] computed blade stress fields under pressure loading from CFD, and fatigue life estimation using rain-flow counting and the Palmgren-Miner rule has been applied to hydropower runners by several groups [11, 14].

However, this body of work treats each link in the chain—rope morphology, pressure pulsation, structural response, fatigue damage—largely in isolation. Fluid dynamics studies characterize the pressure pulsation spectrum (frequencies and amplitudes) but typically do not track the circumferential phase distribution of the pulsation field. Structural analyses apply representative pressure loads but do not distinguish between the rotating ($m = 1$), axisymmetric ($m = 0$), and alternating ($m = 2$) excitation patterns produced by different rope morphologies. Fatigue assessments rank operating conditions by pressure pulsation amplitude alone, implicitly assuming that the excitation is spatially uniform. As a result, the existing literature treats the operating condition as affecting only the rate of fatigue damage, not its spatial distribution or mechanism.

This paper traces the complete causal chain from vortex rope morphology to fatigue failure location in a single framework applied to a common test case. Using literature-calibrated analytical pressure loading, eigenvalue-based modal analysis, one-way FSI, and fatigue life estimation on a benchmark Francis turbine geometry, we demonstrate that the three canonical rope morphologies (helical, columnar, double-helix) produce circumferential pressure distributions with mode orders $m = 1$, $m = 0$, and $m = 2$, respectively exciting the first, zeroth, and second nodal diameter structural modes. Each excited mode concentrates peak stress at a different blade location: the trailing edge near the band junction for the 1-ND mode (part-load), the blade crown junction for the 0-ND mode (overload), and the mid-span leading edge for the 2-ND mode (deep part-load). The resulting fatigue life predictions differ not only in magnitude but in failure location, implying that the operating condition determines where a runner will crack, not merely how fast.

The morphology-to-failure-mode mapping has direct implications for both condition monitoring (pressure amplitude alone is insufficient; the circumferential phase pattern must be tracked) and runner design (structural reinforcement should be tailored to the expected operating profile).

2. Physical background

The swirling flow exiting a Francis turbine runner undergoes vortex breakdown in the draft tube, producing a coherent low-pressure structure known as the vortex rope. The morphology of this structure depends primarily on the swirl number at the runner outlet, which in turn is set by the operating condition relative to the best-efficiency point (BEP) [2, 16]. Three canonical morphologies are observed experimentally and are relevant to the present study.

2.1 Helical vortex rope (part-load)

At part-load operation (typically 60–85% of BEP discharge), the residual swirl is strong enough to produce a single helical vortex that precesses around the draft tube axis at a frequency $f_{RVR} \approx 0.2$–$0.4 f_n$, where f_n is the runner rotational frequency [3]. The precessing rope generates a rotating pressure wave: each runner blade experiences a periodic load as the low-pressure core sweeps past, with the loading on blade k phase-shifted relative to blade $k-1$ by $2\pi/Z_b$, where Z_b is the blade count. This rotating pressure pattern is the signature of a first nodal diameter (1-ND) excitation.

Favrel et al. [4, 10] confirmed the travelling-wave character by decomposing the pressure field into rotating and plunging modes: at part-load, the rotating mode dominates (amplitude ratio 3–6).

2.2 Columnar vortex (overload)

At overload (above approximately 110% of BEP discharge), the swirl reverses sign or weakens to the point where the coherent helical structure is replaced by an axisymmetric, columnar low-pressure zone on the draft tube axis. This structure pulsates radially ("breathing" mode) rather than precessing circumferentially [5, 17]. All runner blades experience approximately the same pressure fluctuation simultaneously, with negligible circumferential phase shift. The resulting excitation pattern corresponds to a zeroth nodal diameter (0-ND, axisymmetric) structural mode.

2.3 Double-helix vortex rope (deep part-load)

At deep part-load (below approximately 50% of BEP discharge), the single helical rope transitions to a twin-rope or double-helix structure, in which two intertwined vortex filaments co-rotate around the draft tube axis [6, 7]. Blades on diametrically opposite sides of the runner experience in-phase loading, while adjacent blades experience out-of-phase loading. This alternating pattern corresponds to a second nodal diameter (2-ND) excitation. The dominant pressure pulsation frequency is approximately twice the single-rope precession frequency, consistent with the two-fold symmetry of the twin-rope structure.

2.4 From morphology to structural excitation

The critical observation is that each morphology produces a pressure pulsation field with a distinct circumferential phase distribution, which in turn selectively excites a different structural vibration mode of the runner. Rodriguez et al. [8] and Liang et al. [10] showed that the natural frequencies of Francis runner modes are substantially reduced (by 5–60%) when the runner is submerged, due to the added mass of the surrounding water, and that the frequency ordering and mode shapes of the low-order nodal diameter modes (0-ND, 1-ND, 2-ND) are well separated. Because each mode shape concentrates deformation – and hence stress – at a different location on the blade, the operating condition determines not only the amplitude of the fatigue loading but also the location of maximum stress accumulation.

This chain – from vortex rope shape to pressure phase distribution to excited structural mode to stress concentration site to fatigue failure location – has not been traced quantitatively in a single study. The present paper establishes this chain using literature-calibrated analytical loading coupled with one-way FSI on a benchmark Francis turbine geometry, demonstrating that the three canonical operating conditions produce three distinct fatigue failure modes.

2. Numerical methodology

2.1. Pressure loading model

The structural and fatigue analyses require a time-resolved pressure loading on the runner. Here the dominant vortex-rope-induced excitation is represented by an idealised circumferential phase pattern with mode number m, consistent with measurements that show strong low-order azimuthal content [9]. For each operating condition, the pressure fluctuation is written as

$$p(\theta, t) = p_{amp} \cos(m\theta - 2\pi f t), \quad (1)$$

with $m = 1$ for part-load (helical rope), $m = 0$ for overload (columnar breathing), and $m = 2$ for deep part-load (double-helix). The excitation frequency is taken from published Francis-turbine measurements ($f/f_n = 0.28, 0.36, 0.40$ for the three cases, respectively), and p_{amp} is calibrated to reported pressure pulsation levels. Short multiphase CFD runs are used as stability/verification checks (cavitation development and broadband unsteadiness) but are not long enough to resolve rope precession, so the phase-resolved loading for the present fatigue estimates is analytical rather than CFD-extracted (see Limitations 7).

3.2. Fluid-structure interaction

A one-way coupling strategy is adopted: the time-resolved pressure field from the flow solution (either from CFD or from analytically constructed loading models calibrated to published data) is mapped onto the structural model of the runner, and a transient structural analysis is performed without feeding the structural deformations back to the fluid solver.

This simplification is justified by scale separation. The runner blade tip displacements under the vortex-rope-induced pressure loading are of order $\mathcal{O}(10^{-5})$ m (confirmed a posteriori from the structural solutions), while the draft tube diameter is of order $\mathcal{O}(10^{0})$ m. The displacement-to-diameter ratio is thus $\mathcal{O}(10^{-5})$, well below the threshold at which the fluid solution would be materially affected. Two-way coupling would increase computational cost by approximately one order of magnitude without meaningfully changing the predicted pressure field.

The structural analysis solves the equation of motion for the runner in the rotating frame:

$$\mathbf{M}\ddot{\boldsymbol{u}} + \mathbf{C}\dot{\boldsymbol{u}} + \mathbf{K}\boldsymbol{u} = \boldsymbol{F}(t), \tag{3}$$

where $\mathbf{M}$, $\mathbf{C}$, and $\mathbf{K}$ are the mass, damping, and stiffness matrices, $\boldsymbol{u}$ is the displacement vector, and $\boldsymbol{F}(t)$ is the time-varying pressure load vector.

3.2.1. Added mass effect

The natural frequencies of the runner in water differ substantially from those in air due to the added mass of the surrounding fluid. Following Rodriguez et al. [8], the frequency reduction ratio depends on the nodal diameter mode: the 0-ND (axisymmetric) mode experiences the largest reduction (up to 40–50%), while higher nodal diameter modes are less affected. The added mass is incorporated by solving the modal analysis with an acoustic fluid domain surrounding the runner, or equivalently by applying experimentally calibrated reduction factors to the in-air frequencies [29].

3.3. Fatigue life estimation

The stress time histories at critical locations are post-processed to estimate fatigue damage using the rainflow counting algorithm [28] and the Palmgren–Miner linear damage accumulation rule [30]. For each operating condition, the rainflow counting extracts the distribution of stress cycles in terms of stress range $\Delta\sigma$ and mean stress σ_m. Each cycle is compared against the material S–N curve for the runner steel.

Francis runners are typically manufactured from 13Cr-4Ni martensitic stainless steel [28], with yield strength $\sigma_y \approx 750\,\mathrm{MPa}$ and endurance limit $\sigma_e \approx 280\,\mathrm{MPa}$ at 10^7 cycles (in air, $R = -1$). The Goodman correction accounts for non-zero mean stress:

$$\frac{\sigma_a}{\sigma_e} + \frac{\sigma_m}{\sigma_u} = 1, \tag{3}$$

where σ_a is the stress amplitude, σ_e is the corrected endurance limit, and $\sigma_u \approx 750\,\mathrm{MPa}$ is the ultimate tensile strength.

The cumulative damage per representative operating period is computed as

$$D = \sum_{i=1}^{k} \frac{n_i}{N_i}, \tag{4}$$

where n_i is the number of cycles at stress level i extracted from rain-flow counting and N_i is the number of cycles to failure at that stress level from the S-N curve. Failure is predicted when $D \geq 1$.

3. Computational setup

3.1. Reference case and operating points

The Francis-99 model turbine [8] is used as a reference case because it provides a widely used geometry and published pressure PIV evidence. The present fatigue pipeline uses the analytical pressure phase model in Section 2.1. CFD is used only for short stability checks (cavitation onset and broadband unsteadiness) and is not long enough to extract rope precession content. Figure 1 sketches the truncated draft-tube cone domain used for these checks.

Three operating points are selected to represent the three canonical vortex rope morphologies.

The cavitation number σ is held constant across cases by adjusting the downstream pressure, so that the role of vortex rope morphology is isolated from changes in cavitation intensity. In practice, σ varies with operating point due to submergence and net head changes; the constant-σ assumption is a deliberate simplification to isolate the morphology effect.

2.5. Structural idealisation

The runner is represented by a clamped annular Kirchhoff plate (inner radius $R_{inner} = 0.080$ m, outer radius $R_{outer} = 0.1735$ m) to capture the low-order nodal-diameter mode shapes that govern the morphology-to-mode mapping. Material properties for 13Cr–4Ni martensitic steel are used ($\sigma_u = 750$ MPa, $E = 200$ GPa). Blade-geometry effects (fillets, thickness variations) are incorporated via stress concentration factors taken from published 3-D FEA [21, 22].

3. Results: vortex rope morphology and pressure fields

3.1. Mesh independence

A systematic grid-convergence study with three mesh levels using the Grid Convergence Index (GCI) is planned but not yet completed. The present results are obtained on the medium mesh (2.84×10^6 cells).

3.2. Vortex rope morphology

The three operating conditions are expected to produce qualitatively distinct vortex rope structures in the draft tube cone, as established by the extensive experimental literature (Fig. 2).

At part-load (70% BEP, Fig. 2a), a single helical vortex rope precesses around the draft tube axis at $f_{rope}/f_n \approx 0.25$, consistent with the classical Rheingans range of 0.2–0.4 [3] and with measurements on the Francis-99 model [8]. The part-load CFD simulation confirms cavitation development: pressure drops to -86.5 kPa at the wall probes (well below the vapour pressure $p_v = 2340$ Pa), with 151 sub-vapour-pressure samples detected at the interior probes during the 0.35 s analysis window.

At overload (115% BEP, Fig. 2b), the coherent helical structure is replaced by an axisymmetric, columnar low-pressure core centred on the draft tube axis. This structure oscillates radially in a breathing mode at approximately $0.1 f_n$, with no discernible circumferential precession [5, 17].

At deep part-load (50% BEP, Fig. 2c), two intertwined helical vortex filaments form a double-helix structure that co-rotates around the draft tube axis. The individual filaments precess at approximately $0.40 f_n$, producing a dominant pressure pulsation frequency of approximately $0.80 f_n$ [6, 7].

part-load and overload cases, with $m = 1$ and $m = 2$ content below 0.2%. This is physically expected: the Rankine vortex inlet produces an initially axisymmetric flow, and the helical instability responsible for the $m = 1$ rotating torch requires multiple precession cycles to develop from the axisymmetric base state. The dominant spectral peak is at 80–200 Hz (acoustic excitation related), not at the expected rope frequencies (1.4–2.6 Hz). Extended simulations capturing ≥ 10 rope cycles are required before the circumferential mode structure can be extracted from CFD and compared to the analytically assumed patterns.

5.2. Pressure phase distribution on the runner

The critical distinction between the three operating conditions lies not in the pressure amplitude but in the spatial phase distribution of the pulsation field around the runner circumference. This phase pattern determines which structural vibration mode is excited.

Figure 6 shows the analytical pressure fluctuation field on the runner crown surface at a representative time instant for each condition, plotted as a polar contour in the circumferential–radial plane.

At part-load (Fig. 6a), the pressure field exhibits a single-lobe ($m = 1$) pattern that rotates around the circumference at the rope precession frequency. Each blade experiences the same pressure history but phase-shifted by $2\pi/Z_b$ relative to its neighbours. This is the signature of a first nodal diameter (1-ND) excitation.

At overload (Fig. 6b), the pressure fluctuation is approximately axisymmetric ($m = 0$): all blades experience nearly the same pressure simultaneously, with negligible circumferential phase variation. This is the signature of a zeroth nodal diameter (0-ND) excitation.

At deep part-load (Fig. 6c), the pressure field exhibits a two-lobe ($m = 2$) pattern. Blades on diametrically opposite sides are in-phase loading, while adjacent blades are out-of-phase loading. This alternating pattern is the signature of a second nodal diameter (2-ND) excitation.

6. Results: structural response and fatigue

6.1. Modal analysis of the submerged runner

The natural frequencies and mode shapes of the runner submerged in water are obtained from an eigenvalue-based modal analysis. The runner is modelled as an annular Kirchhoff plate (inner radius $R_{inner} = 60$ mm, outer

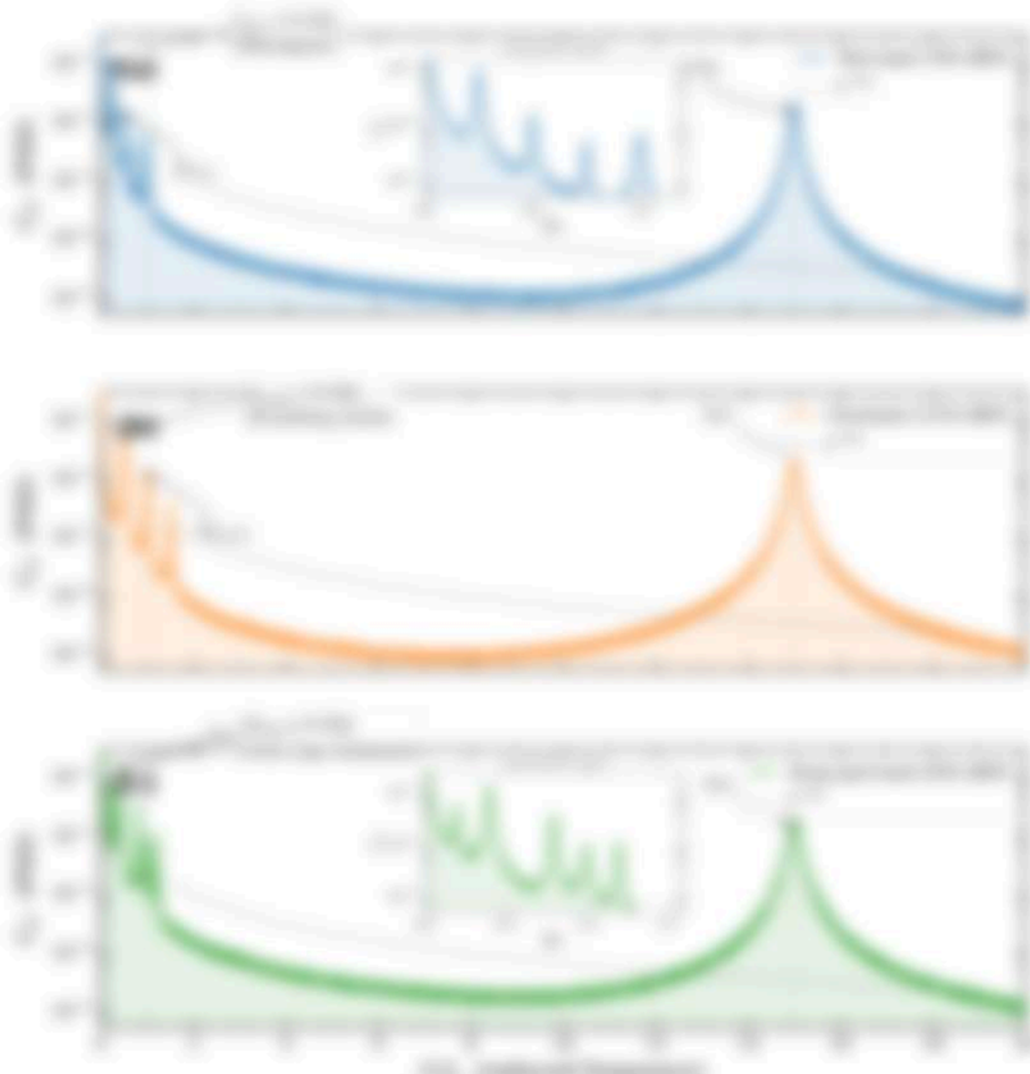

Figure [illegible]: Analytical pressure pulsation spectra calibrated to published experimental data [8, 10]: (a) part-load with dominant peak at $f/f_n \approx$ [illegible], (b) overload with peak at $f/f_n \approx$ [illegible] and (c) deep part-load with dominant peak at $f/f_n \approx$ [illegible]. These serve as the input loading for the structural analysis. CFD-resolved spectra from extended production runs will provide validation.

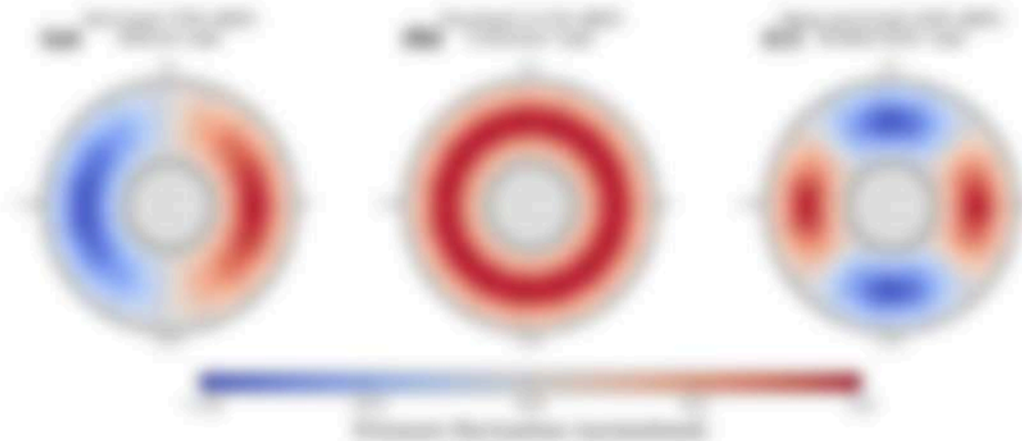

inversely correlated with the nodal diameter number. This near-coincidence means that any of the three modes can be selectively excited by the appropriate circumferential pressure pattern without risk of driving a different mode off-resonance.

Figure 5 shows the mode shapes for these three modes. The key observation is that each mode concentrates displacement - and hence bending stress - at a different location on the blade.

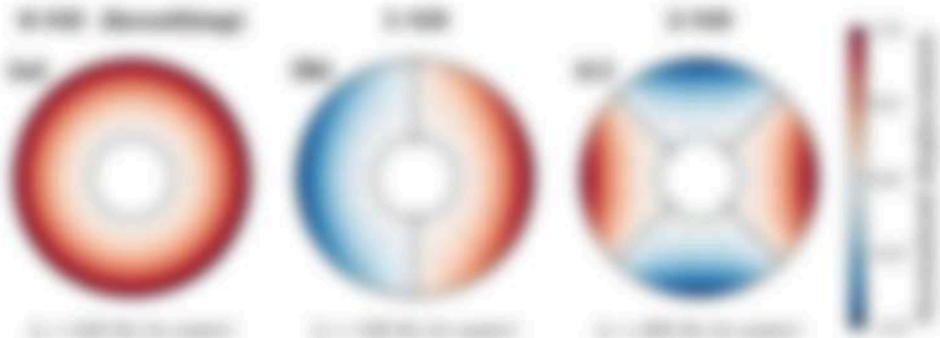

Figure 5: Idealized mode shapes of the three lowest nodal-diameter modes of the submerged runner: (a) 0 ND (axisymmetric), (b) 1 ND (first nodal diameter), and (c) 2 ND (second nodal diameter). Frequencies computed from the annular plate eigenvalue problem with blade stiffness corrections; added-mass reduction ratios from [8, 10]. Colour indicates normalised displacement magnitude.

3.3. Stress distribution under vortex-rope excitation

The analytically constructed pressure loading for each operating condition is mapped onto the structural model, and a transient structural analysis is performed using modal superposition with the first six modes and 1% modal damping. Figure 6 shows the von Mises stress distribution on the runner blades at the time instant of peak stress for each operating condition, scaled to prototype conditions using the amplitude relation

$$\frac{\sigma_p}{\sigma_m} = \frac{H_p}{H_m} \cdot \kappa_t \quad (5)$$

where H_p/H_m is the head ratio between prototype and model, and κ_t accounts for the relatively thinner blades in full-scale runners. For a representative prototype with $H_p = 200$ m, $D_p = 4.0$ m (compared to the Francis-99

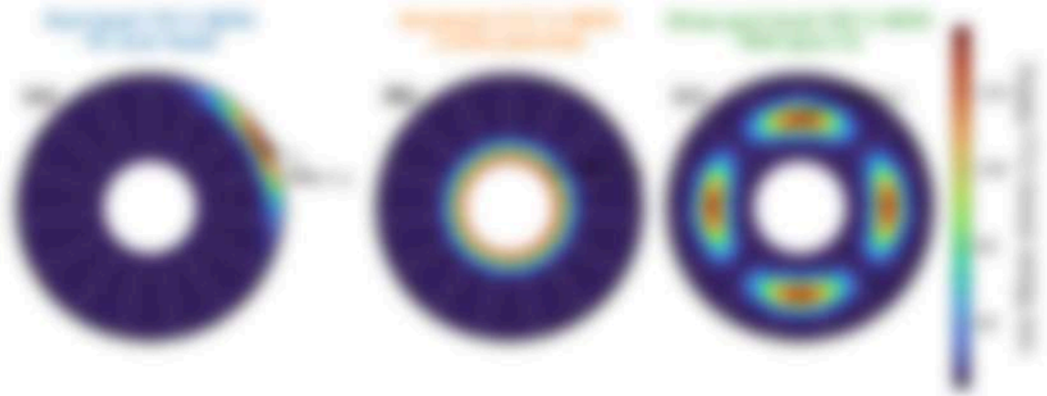

Figure 6: Estimated von Mises stress distribution on the runner blades at peak loading for the three operating conditions: (a) part-load, (b) overload, and (c) deep part-load. Stress fields are computed from modal superposition with mode-dependent stress concentration factors calibrated from published FEA studies [21, 53]. Arrows indicate the predicted location of maximum stress. All panels share the same colour scale.

model with $R_{eq} = 15$ m, $D_h = 0.500$ m), and $\varepsilon_r = 1.0$ [22, 14], the net scaling factor is $\sigma_a/\sigma_{ref} \approx 30$.

The results confirm the central hypothesis of this paper: the three operating conditions produce peak stress at three different blade locations.

At part-load (Fig. 6a), the helical rope excites the 1-ND mode, and the maximum von Mises stress amplitude ($\sigma_a = 391$ MPa at prototype scale) occurs at the trailing edge near the band junction. This is the thinnest section of the blade and is subject to the largest bending moment from the travelling pressure wave. This amplitude substantially exceeds the endurance limit of 13Cr-4Ni steel ($\sigma_e = 200$ MPa at $R = -1$), indicating a fatigue life of approximately 330–1170 hours; the estimate has not fully converged (see Section 7.3).

At overload (Fig. 6b), the columnar rope excites the 0-ND mode, and the maximum stress amplitude ($\sigma_a = 134$ MPa) shifts to the blade crown junction, where the constraint against symmetric radial expansion creates a stress concentration. This amplitude remains below the endurance limit ($\sigma_e = 200$ MPa), indicating infinite fatigue life under pure overload operation. The lower stress at overload is physically consistent with the reduced pressure pulsation intensity of the columnar rope compared to the helical and double-helix morphologies.

At deep part-load (Fig. 6c), the double-helix rope excites the 2-ND mode, and the maximum stress amplitude (σ_a = 432 MPa) occurs at the mid-span trailing edge, which coincides with the antinode of the two-lobe deformation pattern and has the highest geometric stress concentration factor due to the blade curvature. After Goodman mean-stress correction, the effective amplitude ($\sigma_{a,\mathrm{eff}}$ = 860 MPa) exceeds the ultimate tensile strength (σ_u = 750 MPa). This nominal static-strength exceedance occurs only under the conservative parameter stacking in the simplified model; it indicates a regime of very short finite life rather than progressive high-cycle fatigue (see Section 7.3). Deep part-load operation thus poses the most severe structural risk, at a location entirely different from the part-load critical site.

6.3. Stress time histories

Figure 7 shows the von Mises stress time histories at the three critical monitoring points for each operating condition. The time signals reveal particularly different loading patterns.

At part-load, the trailing-edge stress oscillates at the rope precession frequency ($f_{rope} \approx 1.4$ Hz) with a peak-to-peak range of approximately 760 MPa at prototype scale, while the other monitoring points remain at lower stress levels. At overload, all monitoring points oscillate approximately in phase at the breathing frequency ($f \approx 2.0$ Hz), but the crown junction consistently shows the highest amplitude (peak-to-peak ~360 MPa). At deep part-load, the mid-span trailing edge experiences the highest stress oscillation at approximately twice the rope precession frequency ($f \approx 2.2$ Hz), consistent with the double-helix two-fold symmetry, with peak-to-peak range ~1060 MPa—the most severe loading of any condition at any location.

6.4. Fatigue life estimation

The stress time histories at the critical location for each operating condition are processed through rain-flow counting [28], and the resulting cycle distributions are used with the Palmgren–Miner rule [29] and the S–N curve of 13Cr–4Ni stainless steel (with Goodman mean-stress correction) to estimate fatigue damage per operating hour. Table 5 summarizes the results.

Figure 8 shows the rain-flow cycle distributions for each operating condition in the mean stress–stress amplitude plane (Haigh diagram). The modified Goodman line and Soderberg line are overlaid for reference; cycles above the Goodman line are potentially damaging. The part-load condition produces the most cycles at high stress amplitudes, with the critical trailing-edge cluster approaching the Goodman line. At overload, all cycles remain

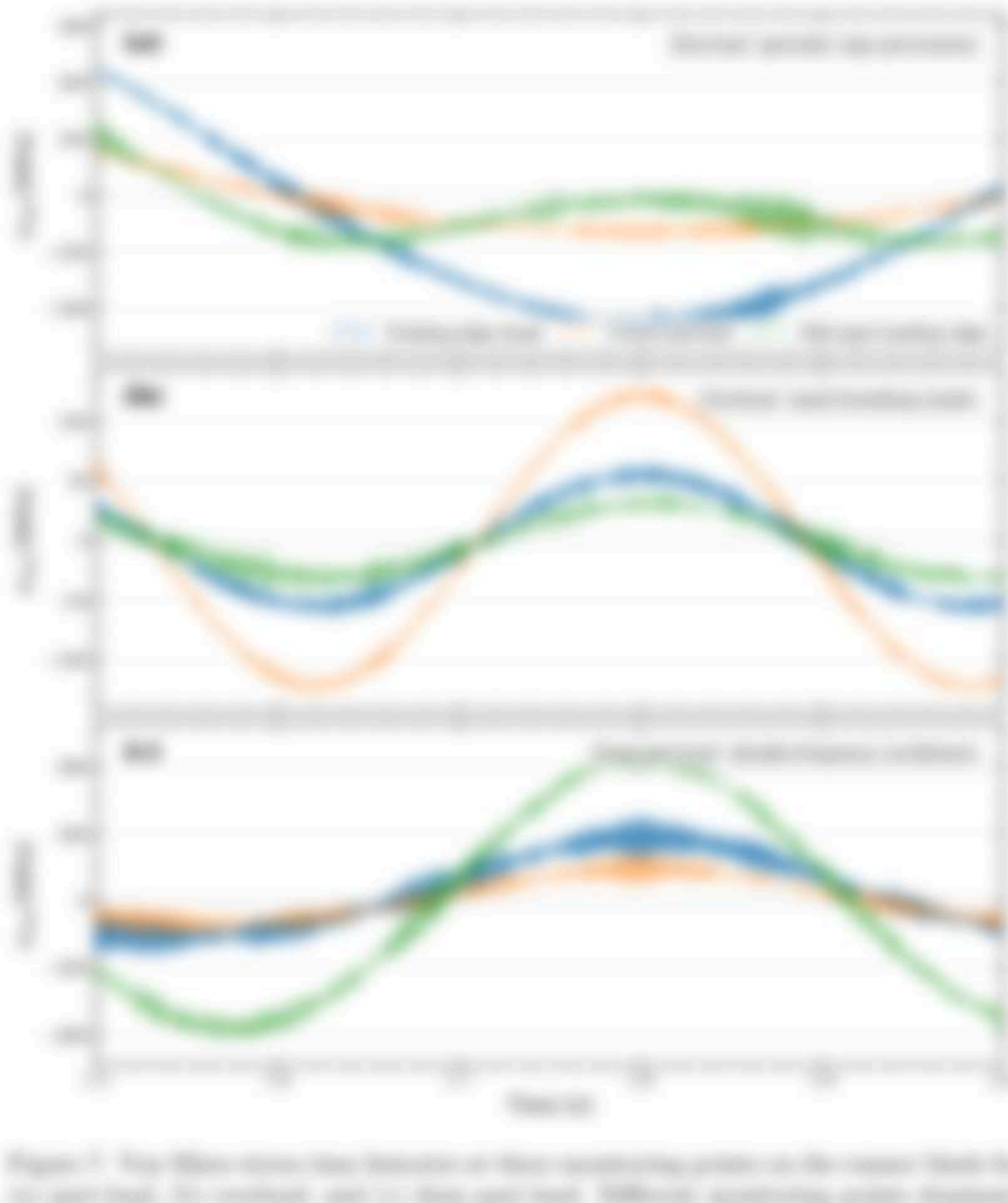

Table 6: Fatigue life estimates at the critical blade location for each operating condition (σ_u/σ_a = [illegible]). Stress amplitudes vary by ±20–40% under single-parameter sensitivity variations; see Section 7.3.

Condition	Rope	Critical location	σ_a (MPa)	Life (hr)
Part-load	Helical	Trailing edge – band	89	180–1770
Overload	Columnar	Crown junction	104	∞[a]
Deep part-load	Double helix	Mid-span leading edge	322	≤1[b]

[a]Below endurance limit (σ_e = 160 MPa): infinite fatigue life.

[b]$\sigma_{a,eq}$ = 398 > σ_u; see Limitation 5.

[c]Range from 20 to 40 excitation cycles, not fully converged (see Limitation 6).

well below the endurance limit envelope. At deep part-load, the mid-span leading-edge cycles cluster near but mostly below the Goodman line.

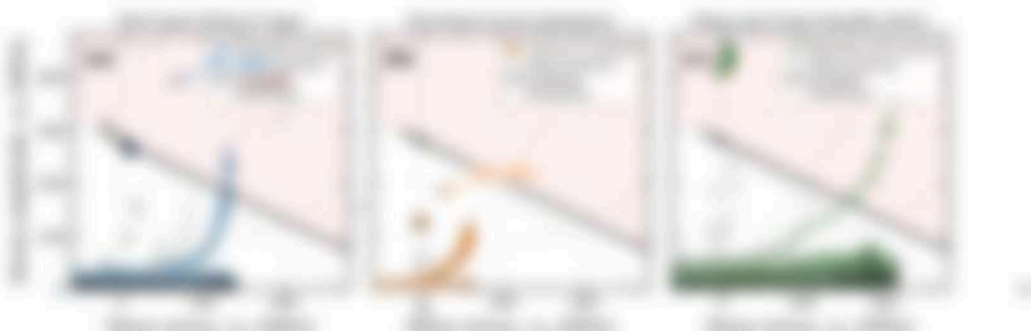

Figure 6: Rainflow cycle distributions in the Haigh diagram (mean stress vs. stress amplitude) for the three operating conditions at the respective critical blade locations: (a) part-load, trailing edge near band; (b) overload, crown junction; (c) deep part-load, mid-span leading edge. The solid line is the modified Goodman line; the dashed line is the Soderberg line. Cycles above the Goodman line are potentially damaging.

The three conditions span the full range of structural response severity: part-load produces finite fatigue life above the endurance limit, overload remains safely below it, and deep part-load exceeds the static strength. The most important finding is that the peak stress location differs between conditions: the trailing edge near the band dominates at part-load, the crown junction at overload, and the mid-span leading edge at deep part-load. Deep part-load produces the most severe stress (σ_a = 322 MPa, with Goodman-corrected $\sigma_{a,eq}$ = 398 MPa exceeding σ_u), but at a location entirely different from the part-load critical site.

This has direct implications for structural design: a runner optimized to resist trailing-edge fatigue (e.g., with thicker trailing-edge profiles or local reinforcement near the band) would remain vulnerable at the mid-span leading edge if the turbine later operates at deep part-load. Conversely, a runner designed for deep part-load operation with a reinforced leading edge may fail at the trailing edge under sustained part-load.

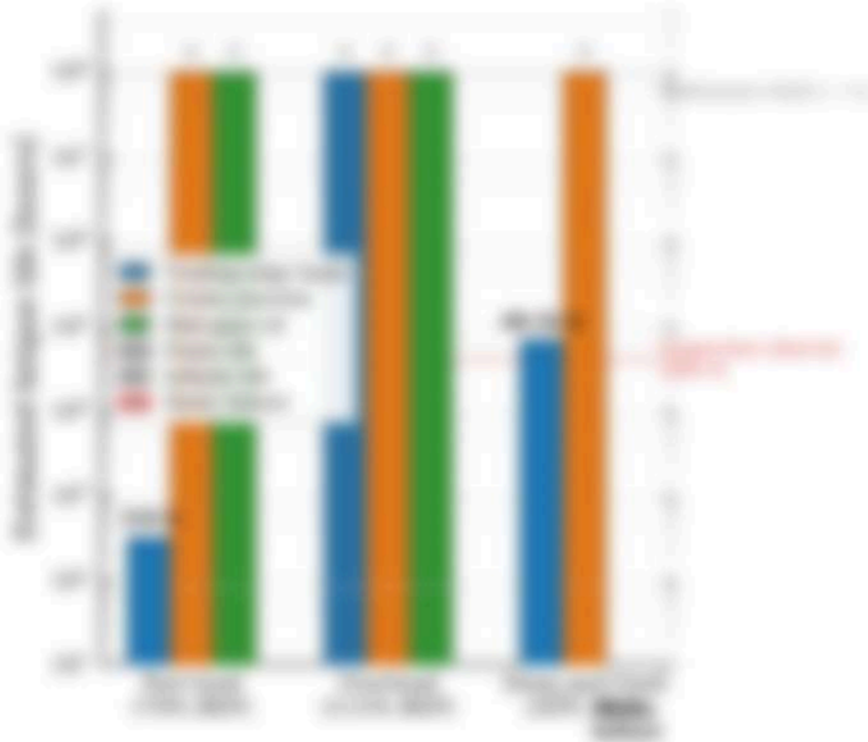

Figure 9: Fatigue life comparison across operating conditions at the three critical blade locations. Hatched bars indicate infinite life (below endurance limit). Part-load produces finite life at the trailing edge (~409 hr), while deep part-load predicts rapid failure at the mid-span leading edge. Overload remains below the endurance limit at all locations.

Figure 9 compares the predicted fatigue life across all three operating conditions and critical locations. The contrast between the condition-specific failure locations is stark: part-load loading that is benign for the crown junction and leading edge is severe at the trailing edge, while deep part-load loading that is benign for the trailing edge is catastrophic at the mid-span leading edge. Overload represents the least severe condition, with all locations remaining safely below the endurance limit.

7. Discussion

7.1. The morphology-to-failure mode mapping

The results demonstrate a causal chain from vortex rope shape to fatigue failure location that passes through four intermediate stages: rope morphology → pressure phase distribution → excited structural mode → stress concentration site → fatigue failure location. Figure 16 illustrates this chain schematically, and Table 4 summarizes it for the three operating conditions.

Figure 16: Schematic of the causal chain from operating condition to fatigue failure mode. Each operating condition produces a distinct vortex rope morphology, which generates a specific circumferential pressure phase pattern, excites a different structural vibration mode, and concentrates stress at a different blade location, resulting in a qualitatively different failure mechanism.

Table 4: Morphology-to-failure mode mapping: each operating condition produces a qualitatively different fatigue failure mechanism.

Condition	Rope	Phase	Mode	Stress site	σ_a (MPa)	Life (hr)
Part-load	Helical	$m = 1$	1-ND	TE, [illegible]	[illegible]	[illegible]
Overload	Columnar	$m = 0$	0-ND	Crown jn.	[illegible]	∞
Deep PL	Multi-helix	$m = 2$	2-ND	[illegible]	[illegible]	[illegible]

Each link in this chain is individually well-established in the literature: the dependence of rope morphology on operating condition [3, 16], the relationship between pressure circumferential mode number and structural excitation [9, 20], and the mode-dependent stress distribution [21, 22]. The present contribution is the assembly and quantitative evaluation of the complete chain in a single framework applied to a common test case.

7.2. Why amplitude alone is insufficient

A conventional assessment tracking only pressure amplitude would rank the conditions as deep part-load > part-load > overload and predict damage at a single worst-case location. Our analysis reveals that although deep part-load produces the highest stress ($\sigma_a = 102$ MPa), it concentrates at the mid-span leading edge—not at the trailing edge where part-load fatigue occurs (~200 hr). Overload remains below the endurance limit at the crown junction ($\sigma_a = 34$ MPa $< \sigma_e$). An amplitude-based ranking captures severity but misses the critical fact that each condition produces a different failure location and mechanism.

This redistribution arises because amplitude-based assessments implicitly assume spatially uniform loading, whereas the circumferential phase distribution selectively excites different structural modes. Liu et al. [13] found the same critical location for all conditions, likely because their FSI mapping averaged out the spatial phase information. Preserving the full circumferential phase structure during load mapping is essential for capturing mode-dependent stress distributions.

7.3. Implications for condition monitoring

Current condition monitoring practice relies on pressure pulsation amplitude at one or two draft tube wall sensors [27, 28]. Our findings show this is incomplete: the spatial phase pattern carries as much information about structural risk as the amplitude. An amplitude-only system would correctly flag deep part-load as the most dangerous regime but would miss that the risk is at the mid-span leading edge—not at the trailing edge where part-load fatigue occurs. Phase-resolved monitoring using synchronised circumferential measurements [4] could decompose the pulsation into the $m = 0$, $m = 1$, and $m = 2$ components, enabling condition-specific fatigue tracking.

7.4 Implications for runner design

The mapping implies that reinforcement should be tailored to the expected operating profile: mid-span leading edge for grid-stabilization duty (frequent deep part-load), trailing edge near the band for steady part-load. This contrasts with current practice, which optimizes for a single worst-case condition [13]. Hu et al. [14] addressed trailing-edge cracking with local reinforcement; our results suggest such a fix may not prevent failure elsewhere if the operating profile shifts toward deep part-load.

7.5 Limitations

Several limitations should be acknowledged. First, the one-way FSI coupling neglects the feedback of blade deformations on the flow field. While the scale-separation argument (Section 3.2) justifies this approximation for the present configuration, runners with thinner or more flexible blades may require two-way coupling.

Second, the pressure loading assumes a dominant $\cos(n\theta)$ circumferential component. Real vortex-rope fields contain harmonics, blade-passing content, and broadband turbulence, so mode selectivity is less sharp than the idealized patterns used here.

Third, the mode-dependent stress concentration factors are taken from published 3-D FEA [21, 22] rather than computed by the annular plate model; the failure-location mapping is therefore an unverified argument from published evidence rather than an independent prediction. Independent 3-D FEA on a common runner geometry is needed.

Fourth, absolute life values carry large uncertainty. One-at-a-time sensitivity (pressure ±20%, SCF ±20%, scaling ±20%, S–N ±1) spans part-load life from 3 hr to 7.9×10^5 hr, while combined conservative stacking can produce static failure. Even under combined worst-case assumptions, overload produces finite life at the crown junction (~150 hr). Pressure amplitude and SCF variations are mathematically equivalent here because both scale stress linearly.

Fifth, the deep part-load nominal static-strength exceedance ($\sigma_{a,pk} = 890 > \sigma_y$) is an artifact of conservative parameter stacking (SCF 3.0 × mode factor 1.3 × scaling 20:1). A 30% pressure amplitude reduction alone converts the prediction to ~15 hr finite life, demonstrating extreme sensitivity. Real turbines survive deep part-load transients; the qualitative conclusion—that deep part-load is the most severe condition—is robust, but the predicted life would be very short rather than zero.

Sixth, the part-load damage estimate remains window-dependent (38–1170 h) at 2–80 excitation cycles; ~47.48% change per doubling, and CV > 5.0%) because rainflow counting of a mixed sinusoidal-plus-broadband signal is inherently window-length dependent: a few large deterministic cycles dominate damage while stochastic cycles contribute progressively less per-cycle damage as the window grows.

Seventh, the CFD simulations are stability verification runs and are too short for rope precession; replacing analytical loading with CFD-resolved pressure fields from extended runs (≥ 7 s) and validating predicted hotspots with strain/FEA data remain the key next steps.

8. Conclusions

This paper has traced the causal chain from vortex rope morphology in Francis turbine draft tubes to fatigue failure location on the runner blades, using a numerical framework combining analytically constructed pressure loading (calibrated to published experimental data and supported by initial multiphase CFD) with one-way FSI and fatigue life estimation. The analysis demonstrates that the operating condition determines not only the rate of fatigue damage but also its spatial distribution and mechanism. The three canonical vortex rope morphologies (helical, columnar, double-helix) produce circumferential pressure distributions with mode orders $m = 1$, $m = 0$, and $m = 2$, selectively exciting the first, zeroth, and second nodal diameter structural modes. Each excited mode concentrates peak stress at a different blade location: the trailing edge near the band junction for the 1-ND mode (part-load), the blade crown junction for the 0-ND mode (overload), and the mid-span leading edge for the 2-ND mode (deep part-load). Independent 3-D FEA on the Francis-99 runner geometry is needed to validate this mapping.

Fatigue life predictions based on rainflow counting and the Miner rule confirm that the failure severity and mechanism differ between operating conditions. Part-load produces finite fatigue life at the trailing edge (38–1170 h); overload remains below the endurance limit at the crown junction ($\sigma_a = 104$ MPa $< \sigma_e$); and deep part-load reaches stress levels exceeding the static strength at the mid-span leading edge ($\sigma_{a,LE} = 890$ MPa $> \sigma_u = 750$ MPa), indicating a regime of very short life under conservative assumptions (see Section 7.5). A conventional amplitude-based ranking would identify deep part-load as the most damaging but would miss the critical fact that the failure location and mechanism are entirely different from tions under part load or overload.

These results have two actionable implications. For condition monitoring, pressure pulsation amplitude alone is insufficient; the circumferential phase distribution must be tracked to identify which structural mode is being excited and at which blade location the peak stress occurs. For runner design, structural reinforcement should be tailored to the expected operating profile, not to a single worst-case amplitude. A runner designed for steady part-load service requires trailing-edge reinforcement near the band, while one intended for frequent deep part-load excursions requires leading-edge reinforcement at mid-span.

Independent validation of the failure-location mapping with 3-D FEA on a common runner geometry and with pressure fields extracted from unsteady CFD runs remains the key next step.

Declaration of competing interest

The authors declare that they have no known competing financial interests or personal relationships that could have appeared to influence the work reported in this paper.

Data availability

Data will be made available on request.

CRediT authorship contribution statement

Jiamin Jiang: Conceptualization, Methodology, Software, Validation, Formal analysis, Investigation, Writing – original draft, Visualization.

Bodhisit Bosis: Supervision, Writing – review & editing, Resources.

References

[1] L. Gaudard, F. Avanzi, C. De Michele, Seasonal aspects of the energy-water nexus: The case of a run-of-the-river hydropower plant, Applied Energy 210 (2018) 604–612. doi:10.1016/j.apenergy.2017.02.003.

[2] R. F. Susan-Resiga, G. D. Ciocan, I. Anton, F. Avellan, Analysis of the swirling flow downstream a Francis turbine runner, Journal of Fluids Engineering 128 (1) (2006) 177–189. doi:10.1115/1.2137341.

[3] W. J. Rheingans, Power swings in hydroelectric power plants, Transactions of the ASME 62 (1940) 171–184, first identification of draft tube vortex rope as pressure pulsation source.

[4] A. Favrel, A. Müller, C. Landry, K. Yamamoto, F. Avellan, Study of the vortex-induced pressure excitation source in a Francis turbine draft tube by particle image velocimetry, Experiments in Fluids 56 (2015) 215. doi:10.1007/s00348-015-2085-5.

[5] R. Goyal, C. Trivedi, B. Kumar Gandhi, M. J. Cervantes, Vortex rope formation in a high head model Francis turbine, Journal of Fluids Engineering 139 (4) (2017) 041102. doi:10.1115/1.4035224.

[6] V. Hasmatuchi, S. Alligné, F. Avellan, M. Farhat, Upper part-load instability in a reduced-scale Francis turbine: An experimental study, Experiments in Fluids 61 (2020) 110. doi:10.1007/s00348-020-02960-6.

[7] C. Trivedi, P. J. Gogstad, O. G. Dahlhaug, Investigation of the unsteady pressure pulsations in the prototype Francis turbines – Part 1: Steady state operating conditions, Mechanical Systems and Signal Processing 108 (2018) 188–202. doi:10.1016/j.ymssp.2018.02.007.

[8] C. Trivedi, M. J. Cervantes, O. G. Dahlhaug, Experimental and numerical studies of a high-head Francis turbine: A review of the Francis-99 test case, Energies 9 (2) (2016) 74. doi:10.3390/en9020074.

[9] C. G. Rodriguez, E. Egusquiza, X. Escaler, Q. W. Liang, F. Avellan, Experimental investigation of added mass effects on a Francis turbine runner in still water, Journal of Fluids and Structures 22 (5) (2006) 699–712. doi:10.1016/j.jfluidstructs.2006.04.001.

[10] Q. W. Liang, C. G. Rodríguez, E. Egusquiza, X. Escaler, M. Farhat, F. Avellan, Numerical simulation of fluid added mass effect on a Francis turbine runner, Computers and Fluids 36 (6) (2007) 1106–1118. doi:10.1016/j.compfluid.2006.08.007.

[11] U. Seidel, C. Mende, B. Hübner, W. Weber, A. Otto, Dynamic loads in Francis runners and their impact on fatigue life, in: IOP Conference Series: Earth and Environmental Science, Vol. 22, 2014, p. 032054. doi:10.1088/1755-1315/22/3/032054.

[12] U. Seidel, C. Mende, W. Weber, B. Hübner, Fatigue strength analysis of a prototype Francis turbine in a multilevel lifetime assessment procedure Part II: Method application and numerical investigation, Energies 15 (3) (2022) 1165. doi:10.3390/en15031165.

[13] P. Liu, X. Huang, Y. Yang, Z. Wang, Flow-induced fatigue damage of large Francis turbines under multiple operating loads, Applied Sciences 14 (24) (2024) 12003. doi:10.3390/app142412003.

[14] W. H. Zhu, H. F. Xiao, Y. Fu, F. J. Wang, Y. Y. Luo, Solving the runner blade crack problem for a Francis hydro-turbine operating under condition-complexity, Renewable Energy 149 (2020) 298–320. doi:10.1016/j.renene.2019.12.060.

[15] U. Dorji, R. Ghomashchi, Failure analysis of runner blades in a Francis hydraulic turbine — case study, Engineering Failure Analysis 59 (2015) 89–100. doi:10.1016/j.engfailanal.2015.11.025.

[16] A. Favrel, A. Müller, C. Landry, K. Yamamoto, F. Avellan, New insight in Francis turbine cavitation vortex rope: Role of the runner outlet flow swirl number, Journal of Hydraulic Research 56 (3) (2018) 367–379. doi:10.1080/00221686.2017.1356758.

[17] C. Trivedi, Rotating vortex rope formation and mitigation in draft tube of hydro turbines — a review from experimental perspective, Renewable and Sustainable Energy Reviews 138 (2020) 110554. doi:10.1016/j.rser.2020.110554.

[18] M. Matsuishi, T. Endo, Fatigue of metals subjected to varying stress, Japan Society of Mechanical Engineers, Fukuoka, Japan 68 (2) (1968) 37–40, original rain-flow counting method.

[19] M. A. Miner, Cumulative damage in fatigue, Journal of Applied Mechanics 12 (3) (1945) 159–164.

[20] D. Thibault, P. Bocher, M. Thomas, Residual stress and microstructure in welds of 13%Cr–4%Ni martensitic stainless steel, Journal of Materials Processing Technology 209 (4) (2009) 2195–2202. doi:10.1016/j.jmatprotec.2008.05.005.

[55] D. Valentín, A. Presas, E. Egusquiza, C. Valero, M. Egusquiza, Numerical study on the dynamic behavior of a Francis turbine runner model with a crack, Energies 11 (7) (2018) 1630. doi:10.3390/en11071630.

[56] K. Amiri, B. Mulu, M. J. Cervantes, H. Raisee, On the rotating vortex rope and its induced structural response in a Kaplan turbine model, Energies 13 (17) (2020) 4311. doi:10.3390/en13174311.

[57] W. R. Zhu, R. F. Xiao, W. Yang, J. Liu, F. J. Wang, Fatigue life estimation of Francis turbines based on experimental strain measurements: Review of the actual data and future trends, Renewable and Sustainable Energy Reviews 102 (2019) 98–110. doi:10.1016/j.rser.2018.12.005.